Supporting Information

Modular design of efficient heterostructural FeS_2/TiO_2 oxygen evolution electrocatalyst via sulfidation of natural ilmenites

Zhijie Chen,[a,b,1] Renji Zheng,[a,1] Shimao Deng,[a] Wenfei Wei,[a] Wei Wei,[b] Bing-Jie Ni[b,*] and Hong Chen[a,*]

[a] *State Environmental Protection Key Laboratory of Integrated Surface Water-Groundwater Pollution Control, Shenzhen Key Laboratory of Interfacial Science and Engineering of Materials (SKLISEM), School of Environmental Science and Engineering, Southern University of Science and Technology, Shenzhen 518055, PR China*

[b] *Centre for Technology in Water and Wastewater, School of Civil and Environmental Engineering, University of Technology Sydney, NSW 2007, Australia*

*Corresponding Authors:

Bing-Jie Ni E-mail: bingjieni@gmail.com

Hong Chen E-mail: chenh3@sustech.edu.cn

Z. Chen and Dr. R. Zheng contributed equally to this work.

Experimental section

Catalyst synthesis

The S-FTO catalyst was synthesized by a two-step mechanical milling-sulfidation method. Briefly, the high-purity ilmenite ores obtained from Yunan, China were first mechanically milled in a planetary mill (QM-3SP04) for 2 h, with a speed of 540 r min^{-1}. After that, the resulting particles (FTO) were thermally sulfidized in a tube furnace. Specifically, an alumina boat containing a certain amount of sulfur powder (5 g) was located at the upstream position, while 10 g of the FTO particles were placed in the centre of the tube. The mass ratio of FTO and sulfur powder was controlled as 2:1. The thermal sulfidation reaction was performed with argon (50 sccm) as carrier gas. The furnace temperature was kept at 450 °C (with a heating rate of 5 °C min^{-1}) and maintained for 4 h. After furnace cooling to room temperature, the sample was washed with ethanol and deionized water and dried in a vacuum drying oven to obtain S-FTO.

The FeS_2 catalyst was synthesized by a mechanical milling method. Briefly, the high-purity natural pyrite ores obtained from Guizhou, China (**Table S4**) were mechanically milled in a planetary mill (QM-3SP04) for 2 h, with a speed of 540 r min^{-1}. After that, the resulting particles were collected and washed with ethanol and deionized water and dried in a vacuum drying oven to obtain the FeS_2 catalyst.

Physical and chemical characterization

The elemental content of the raw ore was determined by an X-ray fluorescence

spectrometer (XRF, ARL Advant'X Intellipower 3600). The crystal structure of catalysts was determined by X-ray diffraction (XRD) measurements on a Rigaku Smart-Lab 9 kW diffractometer with the X-ray tube operated at 45 kV and 20 mA. The morphology of catalysts was examined with scanning electron microscopy (SEM, Zeiss Sigma 500). The Raman spectra were recorded on a ThermoFisher DXRi Raman microscope. Transmission electron microscopy (TEM) and high-resolution TEM (HRTEM) images were obtained on a TEM instrument (FEI Tecnai G2 F20 S-TWIN) with an acceleration voltage of 200 kV. Energy dispersive spectroscopy (EDS) mapping measurements were conducted by a TEM which is equipped with an EDS. The element composition and surface chemistry of catalysts were tested by the X-ray photoelectron spectroscopy (XPS, Thermo K-Alpha^{+}, Thermo Fisher Scientific, USA) with the Al (K_{α}) radiation. The ion concentrations in the electrolyte were measured by an inductively coupled plasma mass spectrometry (ICP-MS) instrument (Agilent 7700s).

Electrochemical tests

The electrochemical performance of catalysts was tested with a CHI 660E electrochemical workstation with a three-electrode system. Hg/HgO served as the reference electrode, and a graphite rod was the counter electrode. For the preparation of the working electrode, 5 mg of catalyst powder was first dispersed in 1 mL of mixed solution (500 μL of water, 450 μL of ethanol, and 50 μL of 5 wt% Nafion solution). After sonication for about 30 min, a homogeneous ink was obtained. Then, 100 μL of the ink was deposited onto a piece of acid-treated nickel foam (NF, 1×1×0.2 cm^3), and

the catalyst loading was 250 μg cm^{-2}. For comparison, the OER performance of the purchased RuO_2 (99.9%, Aladdin), the FeS_2 catalyst, and the TiO_2 catalyst was also tested. The preparation of the RuO_2 electrode, the FeS_2 electrode, and the TiO_2 electrode also followed the same process as the S-FTO electrode. Before electrochemical tests, the KOH (1 M) electrolyte was saturated by O_2 bubbles for about 15 min. After initial 20 cyclic voltammetric (CV) scans to activate catalysts, linear sweep voltammetry (LSV) curves were recorded at a scan rate of 5 mV s^{-1}, in 1.0 M KOH solution. The polarization curves were calibrated with 90% iR compensation to eliminate the solution resistance. All potentials measured were converted to the reversible hydrogen electrode (RHE) via the following equation: $E_{vs.\ RHE} = E_{vs.\ Hg/HgO} + 0.059\ pH + 0.098$ V. Electrochemical impedance spectroscopy (EIS) was recorded at 1.5 V vs. RHE over the frequency range of 10^{-2} to 10^5 Hz, with an AC signal amplitude of 5 mV. The double-layer capacitances (C_{dl}) were calculated by conducting CVs at different scan rates (i.e., 40, 60, 80, 100, and 120 mV s^{-1}) in 1.0 M KOH. Furthermore, the value of ECSA was calculated by the equation: $ECSA = S * C_{dl} / C_s$, where C_{dl} is the double layer capacitance; C_s is the general specific capacitance, the value is about 0.04 mF cm^{-2} in 1.0 M KOH, and S is the area of the working electrode. To test the long-term stability of catalysts, the chronoamperometric i-t curves were measured for 24 h.

Computational methods

Spin-polarization density functional theory (DFT) calculations were performed using

the Cambridge Sequential Total Energy Package (CASTEP) code[1]. The electron exchange-correlation energy was treated by the generalized gradient approximation (GGA) with Perdew-Burke-Ernzerhof (PBE) functional[2]. Given the strong correlation effect of transition metals, DFT + U method was employed with the value of U_{eff} = 5 and 1 eV for Fe and Ti atoms based on previous studies, respectively[3]. To build the interfacial heterostructure, a specific surface is constructed to make sure the interfacial strain of each interface structure is less than 2 %. For FeS_2@FeOOH heterojunction, a slab model composed of FeOOH (010) surface and FeS_2 (100) surface was constructed. A slab model composed of FeOOH (010) surface and $FeTiO_3$ (001) surface was constructed to simulate the $FeTiO_3$@FeOOH heterojunction. All the atoms in these structures were fully relaxed to using the conjugated gradient method until a convergence criterion of 10^{-5} eV for energy, 1×10^{-3} Å for maximum displacement, and 0.02 eV $Å^{-1}$ for force. A vacuum space of 15 Å was constructed to avoid the interaction between adjacent slabs. The kinetic energy cutoff was set to 500 eV for the plane-wave basis set. For heterojunction surface calculations, Brillouin zone integration was sampled with the 2 × 2 × 1 Monkhorst-Pack mesh k-point. During the geometry optimizations step, the bottom pyrite and ilmenite slabs were constrained at the bulk position and the surface slab was relaxed.

The OER in the alkaline electrolyte ($4OH^- \rightarrow O_2 + 2H_2O + 4e^-$) generally undergoes the following four elementary steps:

$$* + OH^- \rightarrow OH^* + e^- \quad (1)$$

$$OH^* + OH^- \rightarrow O^* + H_2O + e^- \quad (2)$$

$$O^* + OH^- \rightarrow OOH^* + e^- \quad (3)$$

$$OOH^* + OH^- \rightarrow * + O_2 + H_2O + e^- \quad (4)$$

where * denotes a surface-active site; O*, OH*, and OOH* are the reaction intermediates. The Gibbs free energy change for each OER step is calculated as the difference between the free energies of the initial and final states as shown below:

$$\Delta G = \Delta E + \Delta ZPE - T\Delta S \quad (5)$$

where ΔE is the calculated reaction energy by DFT, ΔZPE is the differences in zero-point energies, and ΔS represents the entropy change. Hence, the Gibbs free energy changes for reactions (1) - (4) can be obtained using following equations:

$$\Delta G_1 = G(OH^*) - G(*) - \mu_{OH} = E(OH^*) - E(*) - E(H_2O) + 1/2\, E(H_2) - eU + \Delta G_{pH} + \Delta(ZPE - T\Delta S) \quad (6)$$

$$\Delta G_2 = G(O^*) - G(OH^*) + \mu_H = E(O^*) + 1/2\, E(H_2) - E(OH^*) - eU + \Delta G_{pH} + \Delta(ZPE - T\Delta S) \quad (7)$$

$$\Delta G_3 = G(OOH^*) - G(O^*) - \mu_{OH} = E(OOH^*) - E(O^*) - E(H_2O) + 1/2\, E(H_2) - eU + \Delta G_{pH} + \Delta(ZPE - T\Delta S) \quad (8)$$

$$\Delta G_4 = 4 \times [1.23\ eV - eU + \Delta G_{pH}] - (\Delta G_1 + \Delta G_2 + \Delta G_3) \quad (9)$$

where U is the potential measured against NHE at standard conditions. G_{pH} is the H^+

free energy correction by the concentration dependence of the entropy: $\Delta G_{pH} = -k_B T \ln[H^+]$, where k_B and T are Boltzmann constant and temperature, respectively.

The theoretical overpotential (η) could be calculated from free energy differences at each step as:

$$\eta_{OER} = \max [\Delta G_1, \Delta G_2, \Delta G_3, \Delta G_4]/e - 1.23\ V \quad (10)$$

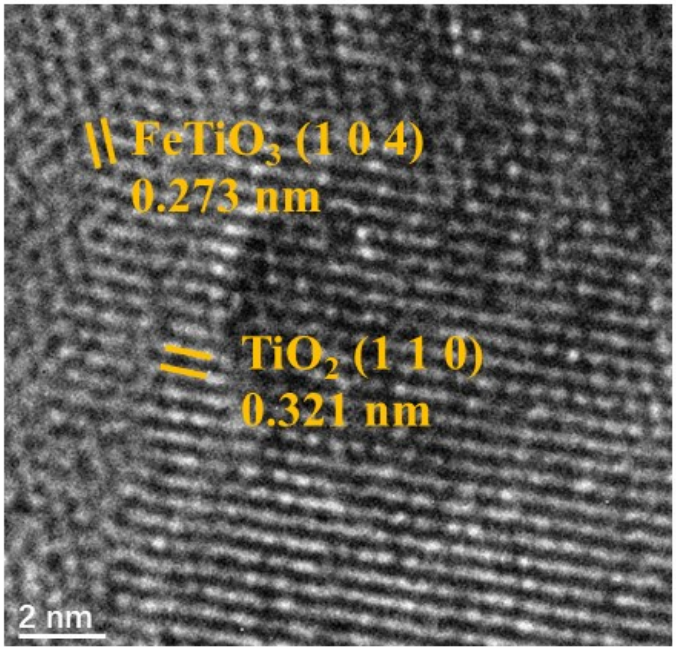

Figure S1. HRTEM image of FTO.

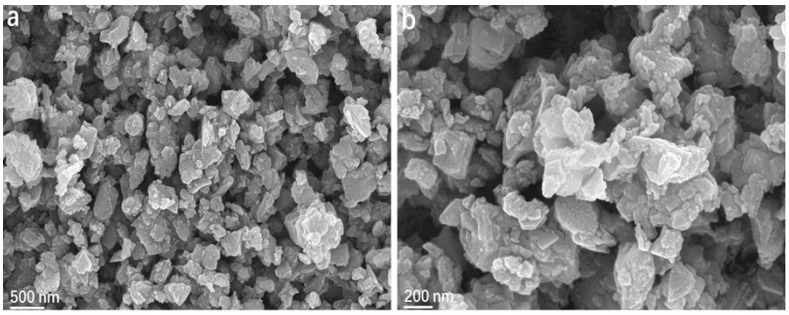

Figure S2. SEM images of S-FTO.

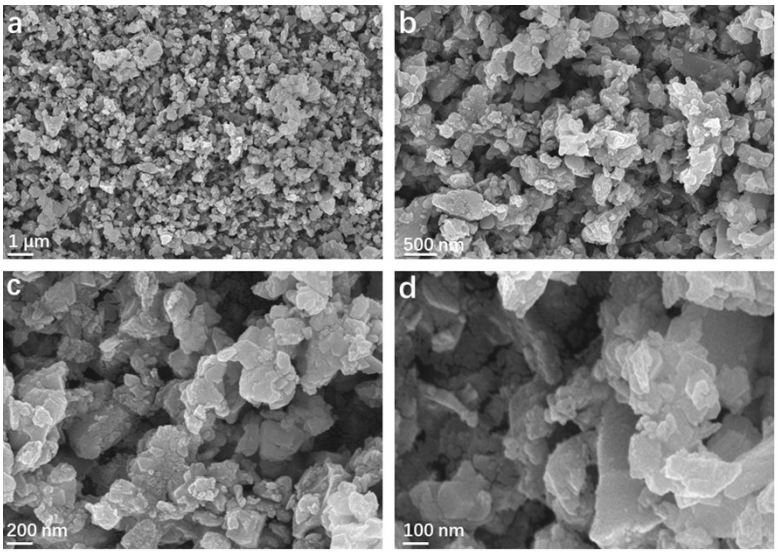

Figure S3. SEM images of FTO.

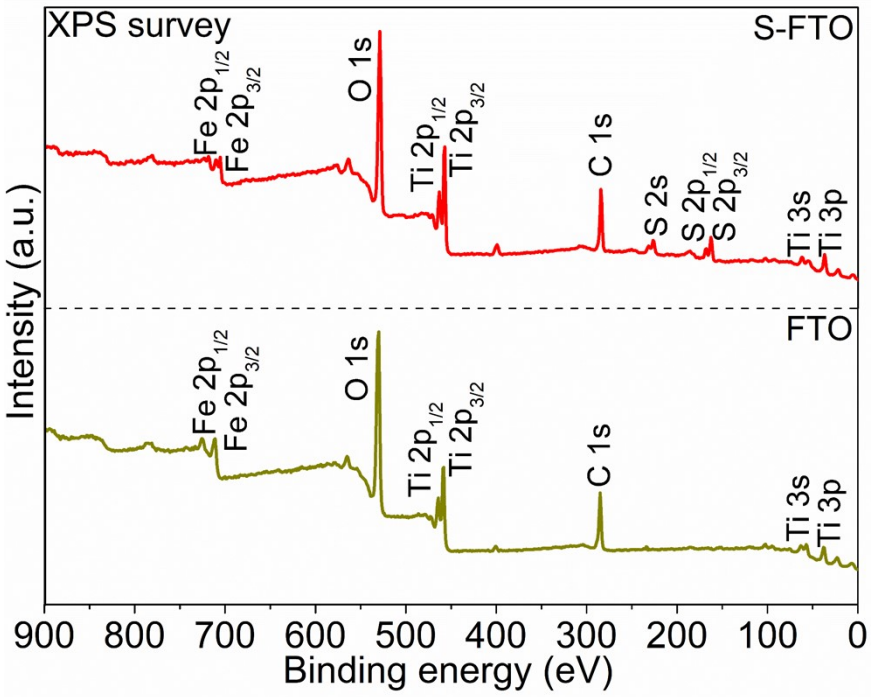

Figure S4. XPS survey of S-FTO and FTO.

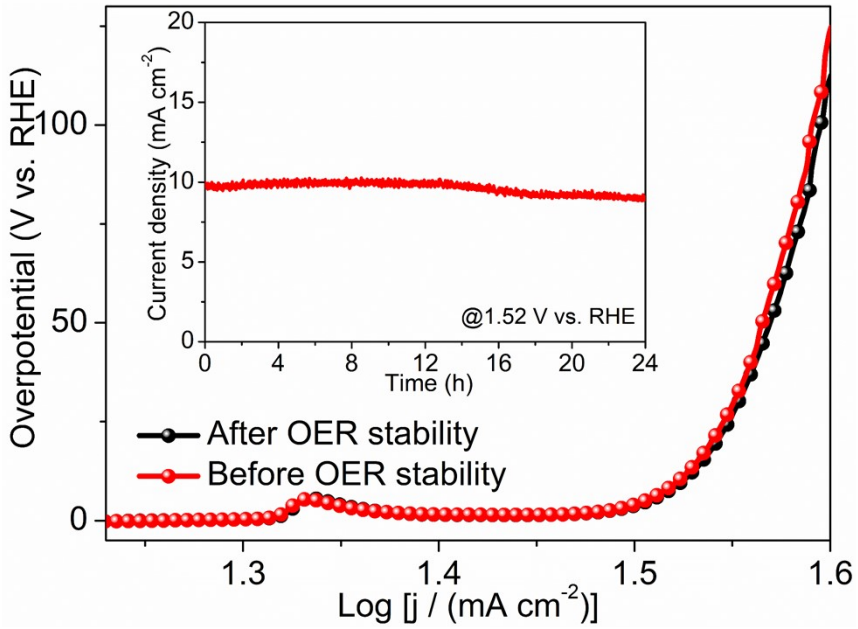

Figure S5. LSV curves of FTO before and after the OER stability test in 1 M KOH, inset is the Chronoamperometric curve of FTO at 1.52 V vs. RHE.

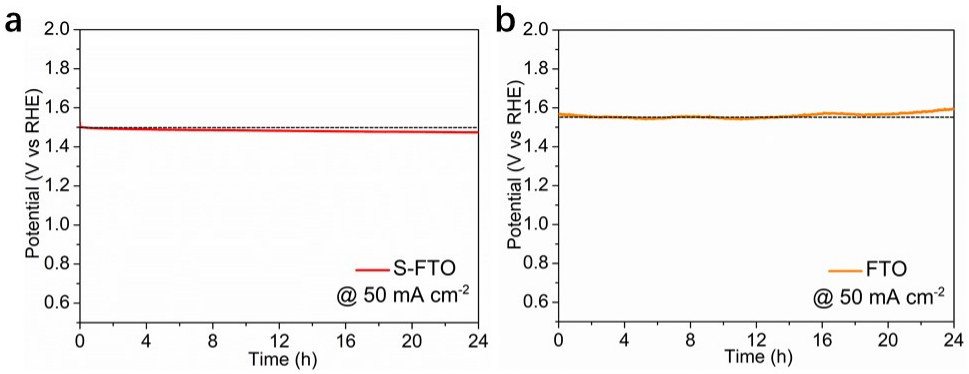

Figure S6. Long-term durability test of (a) S-FTO and (b) FTO at 50 mA cm^{-2}.

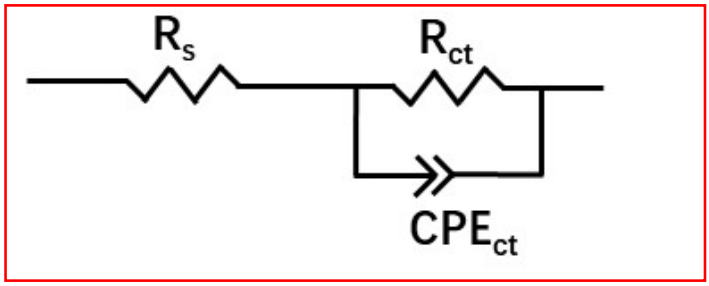

Figure S7. Equivalent circuit model for EIS data fitting.

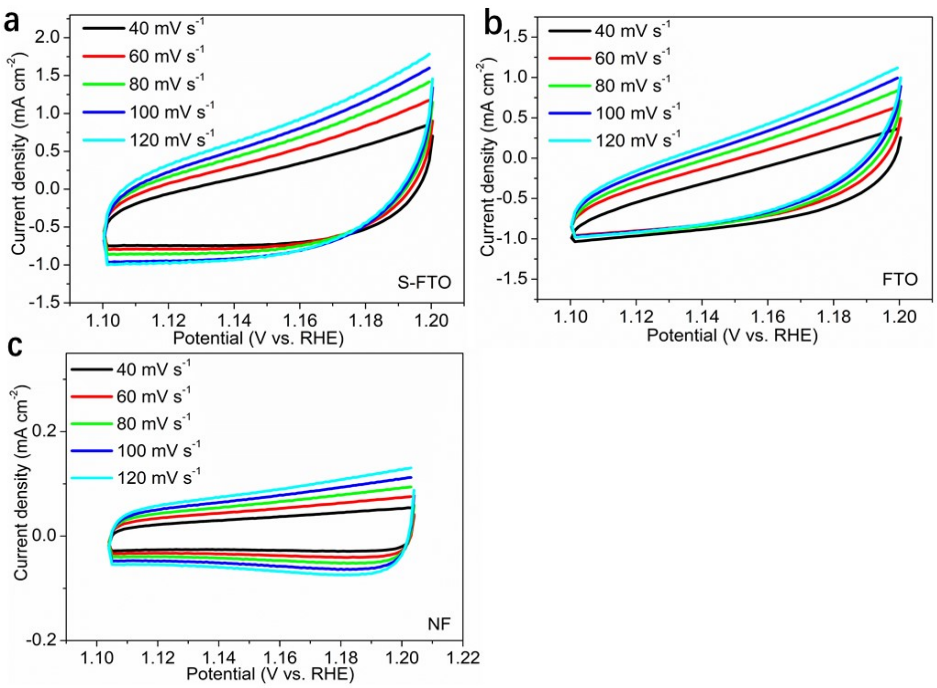

Figure S8. CV curves of (a) S-FTO, (b) FTO, and (C) NF at different rates, in the region of 1.1 ~ 1.2 V vs. RHE.

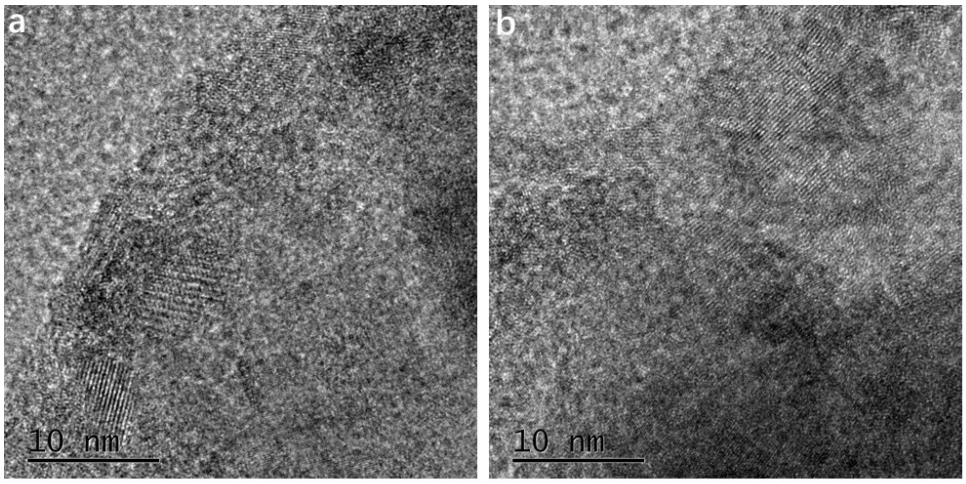

Figure S9. TEM images of S-FTO after the OER test.

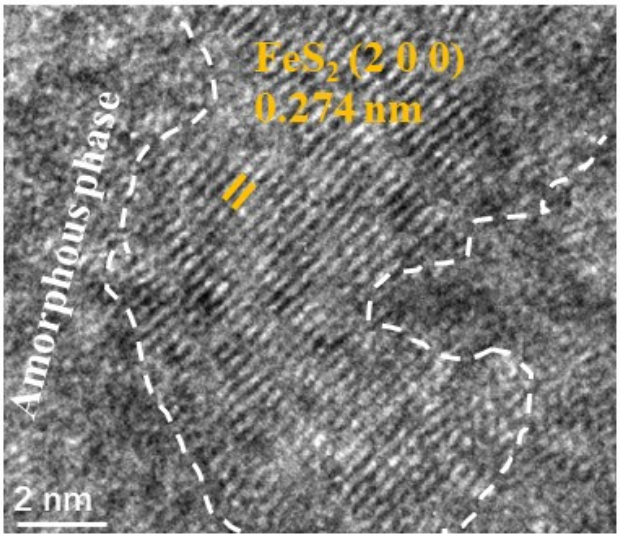

Figure S10. HRTEM images of S-FTO after the OER test.

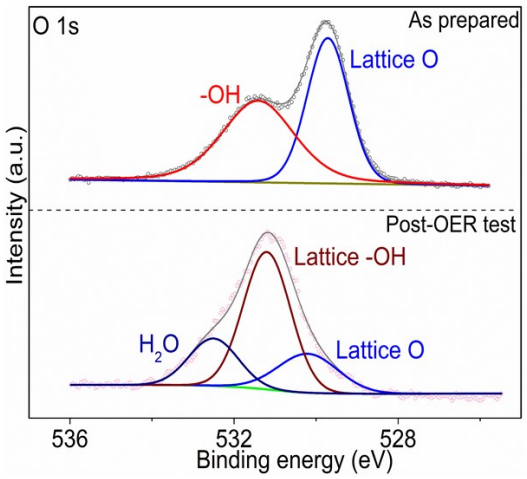

Figure S11. HRTEM images of S-FTO after the OER test. High-resolution XPS scans of S-FTO in the O 1s region before and after the OER test.

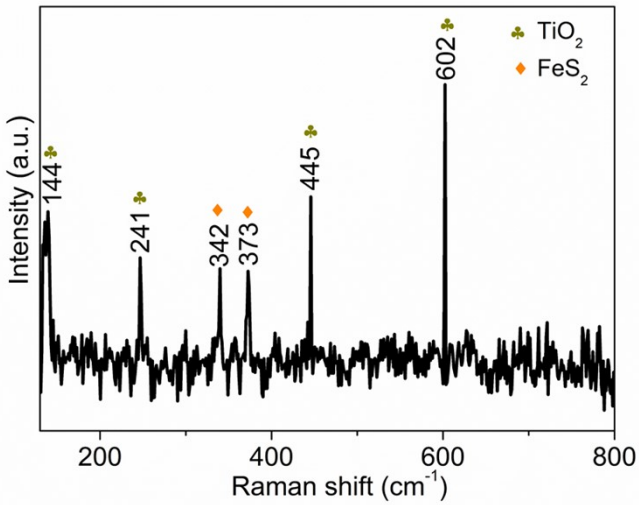

Figure S12. Raman spectrum of as-prepared S-FTO.

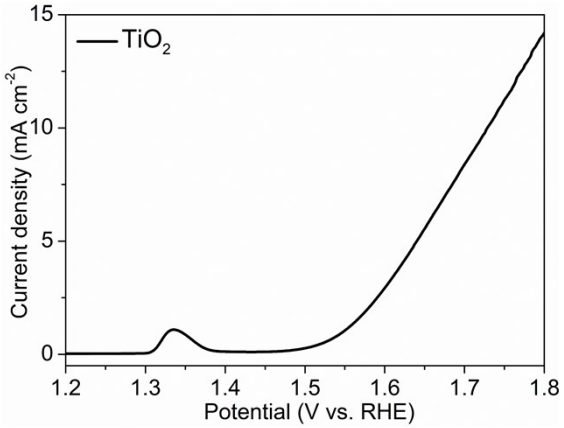

Figure S13. Linear sweep voltammetry curve of high-purity rutile TiO_2 in 1.0 M KOH.

The high-purity rutile ores (**Table S5**) were obtained from Yunan, China. To test the OER performance of the rutile TiO_2, the ore was first milled and then washed with ethanol and deionized water and dried in a vacuum drying oven. The rutile TiO_2 working electrode was prepared with the same process as other working electrodes described in the Experimental section.

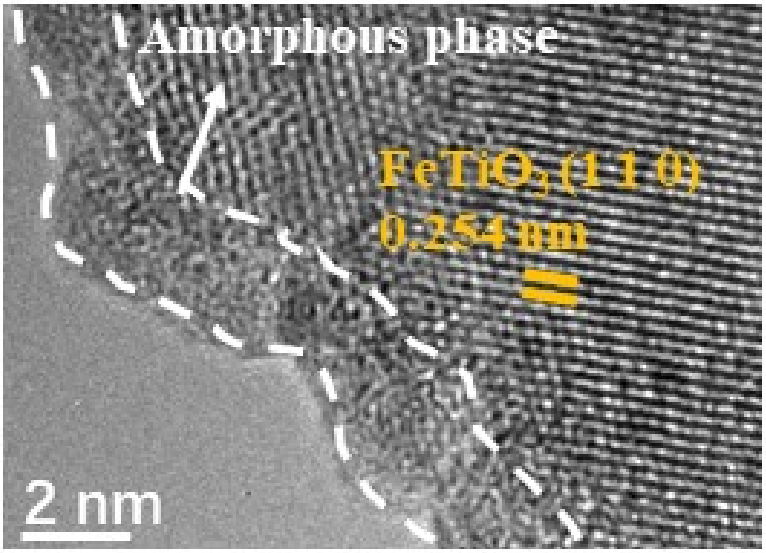

Figure S14. HRTEM image of post-OER FTO.

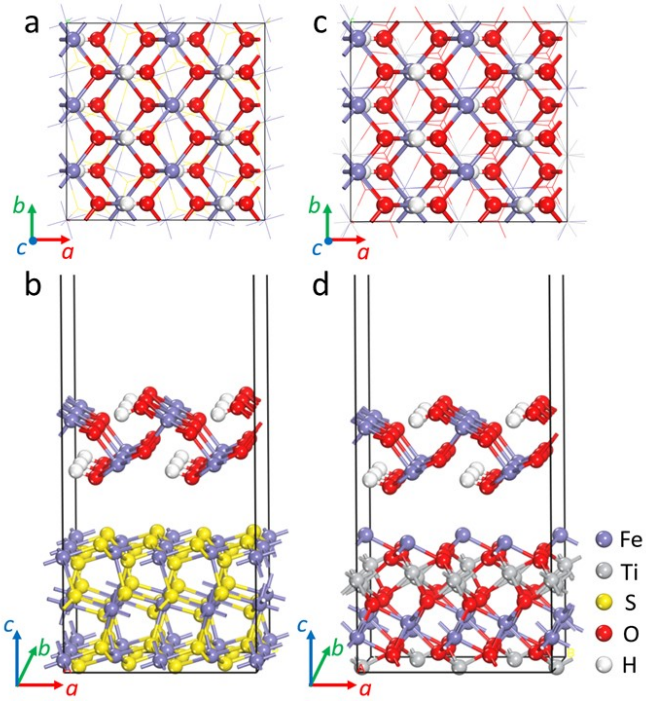

Figure S15. Structure representations of (a, b) FeS_2@FeOOH and (c, d) $FeTiO_3$@FeOOH.

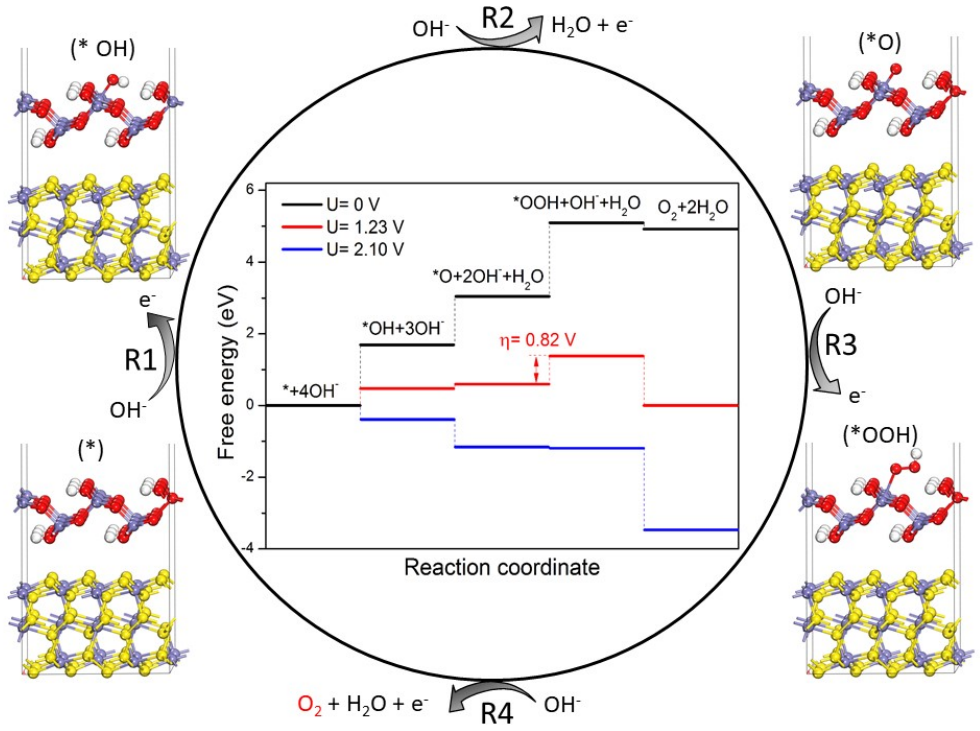

Figure S16. DFT calculated reaction energies of FeS_2@FeOOH with corresponding optimized structures.

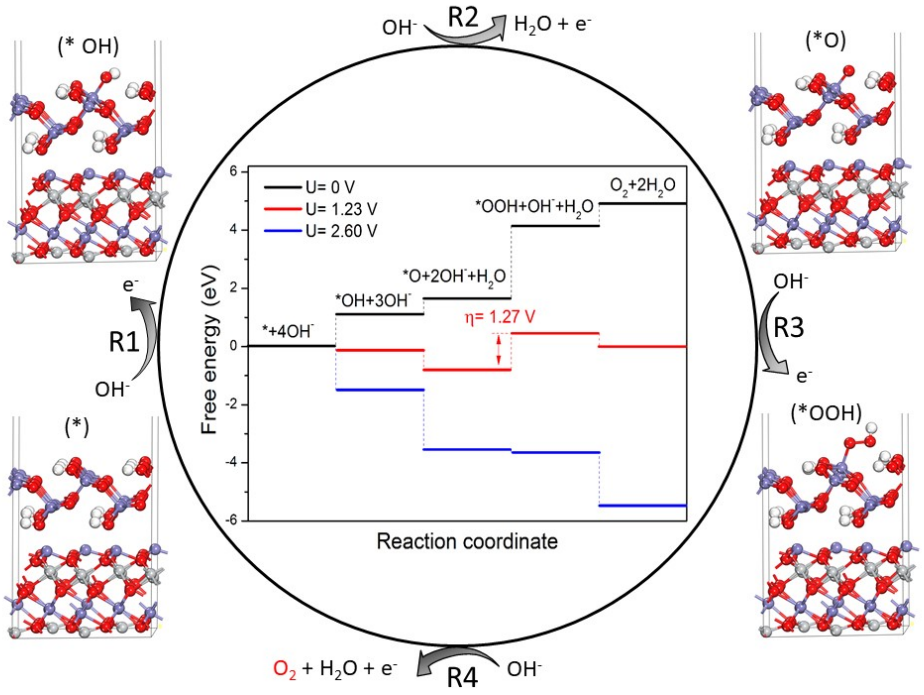

Figure S17. DFT calculated reaction energies of $FeTiO_3$@FeOOH with corresponding optimized structures.

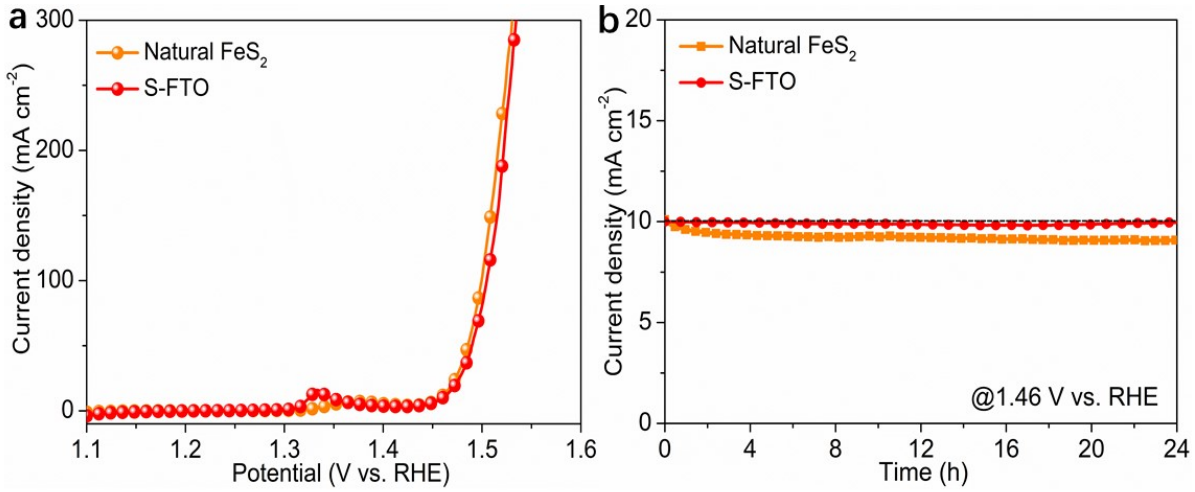

Figure S18. (a) Linear sweep voltammetry curves of S-FTO and natural pyrite in 1.0 M KOH. (b) Chronoamperometric curve of S-FTO and natural pyrite at 1.46 V vs. RHE.

Table S1. Chemical composition of the ilmenite ore.

Component	TiO_2	FeO	SiO_2	K_2O	MgO	MnO	Al_2O_3	CaO
Mass ratio (%)	55.73	42.39	0.84	0.16	0.25	0.19	0.32	0.12

Table S2. A summary of the OER properties of S-FTO and a group of recently documented catalysts.

Catalyst	η_{10} (mV)	Tafel slope (mV dec^{-1})	Reference
Mn_3N_2	270	101	*Angew. Chem. Int. Ed. 2018,57, 698.*
w-$Ni(OH)_2$	237	83	*Nat. Commun. 2019, 10, 1–10.*
HG-NiFe	313	39	*Sci. Adv. 2018, 4, eaap7970.*
Ni-NHGF	330	63	*Nat. Catal. 2018, 1, 63.*
Fe_3O_4/FeS_2-2.5	253	48	*J. Mater. Chem. A 2020, 8, 14145–14151.*
Ni-MoN	276	98	*Adv. Energy Mater. 2018, 8, 1802327.*
S|NiN_x-PC/EG	280	45	*Nat. Commun. 2019, 10, 1392.*
Fe-Mn-O NSs	273	63	*Adv. Funct. Mater. 2018, 28, 1802463.*
NiCoP/C@FeOOH	271	69	*Nanoscale, 2019, 11, 19959–19968.*
Co_3O_4/Co-Fe oxide	297	61	*Adv. Mater. 2018, 30, 1801211.*
$Ni_{0.6}Co_{1.4}P$	300	80	*Adv. Funct. Mater. 2018, 28, 1706008.*
Co_4N@NC	257	58	*ACS Energy Lett. 2020, 5, 692.*
Co_4N/CNW/CC	310	81	*J. Am. Chem. Soc. 2016, 138, 10226.*
NiFe LDH NSA	269	48	*Nat. Commun. 2018, 9, 2609.*
$Co_{0.5}(V_{0.5})$	282	56	*Adv. Energy Mater. 2020, 10, 1903571.*
F-CoOOH/NF	270	54	*Angew. Chem. Int. Ed. 2018 , 57, 15471.*
Co@N-CS/NHCP@CC	248	68	*Adv. Energy Mater. 2019, 1803918.*
3D Co(OH)F	313	52	*Adv. Mater. 2017, 29, 1700286.*
Fe-Co-P-O NBs	268	53	*Energy Environ. Sci. 2019, 12, 3348.*

$CoFe_{0.2}S_x$	320	48	*ACS Catal.* 2020, 10, 1855-1864.
SCFP-NF	310	55	*Adv. Mater. 2018, 30, 1804333.*
Ni_3Se_4@FeOOH	249	46	*Mater. Today Energy 2020, 17, 100462.*
$Ni_{0.75}Mn_{0.25}$ nanosheets	297	91	*ACS Energy Lett. 2018, 3, 2150.*
NiFeMn-LDH	262	47	*Energy Environ. Sci. 2017, 10, 121−128.*
CoFeZr oxides	248	54	*Adv. Mater. 2019, 1901439.*
Au/NiFe LDH	237	36	*J. Am. Chem. Soc. 2018, 140, 3876-3879.*
S-FTO	**230**	**47**	**This study**

Table S3. Calculated charge transfer resistance (R_{ct}) and solution resistance (R_s) (in Ohm, Ω) of the materials deposited on NF obtained from the Nyquist plot during the EIS experiments at 1.5 V vs. RHE.

Catalyst	R_s	R_{ct}
S-FTO	0.9	0.8
FTO	1.1	3.4

Table S4. Chemical composition of the pyrite ore.

Element	Fe	S	Si	Mg	Al	Ca	Others
Mass ratio (%)	44.95	51.84	0.68	0.56	0.22	0.26	1.49

Table S5. Chemical composition of the rutile ore.

Element	TiO_2	SiO_2	Fe_2O_3	MgO	Al_2O_3	Others
Mass ratio (%)	98.24	0.34	0.23	0.11	0.21	0.87

References:

[1] Clark, S. J.; Segall, M. D.; Pickard, C. J.; Hasnip, P. J.; Probert, M. I. J.; Refson, K.; Payne, M. C., First principles methods using CASTEP. Zeitschrift für Kristallographie - Crystalline Mater. 2005, 220 (5-6), 567-570.

[2] Gao, L.; Cui, X.; Wang, Z.; Sewell, C. D.; Li, Z.; Liang, S.; Zhang, M.; Li, J.; Hu, Y.; Lin, Z., Operando unraveling photothermal-promoted dynamic active-sites generation in $NiFe_2O_4$ for markedly enhanced oxygen evolution. Proc. Natl. Acad. Sci. U. S. A. 2021, 118 (7), e2023421118.

[3] Qin, L.; Cheng, Z.; Fan, J. A.; Kopechek, D.; Xu, D.; Deshpande, N.; Fan, L.-S., Nanostructure formation mechanism and ion diffusion in iron–titanium composite materials with chemical looping redox reactions. J. Mater. Chem. A 2015, 3 (21), 11302-11312.